Numerical Investigation of Two-Dimensional Compressible Shear Layer and Comparison to Weakly Compressible Model

By M. Rennie, Z. Ponder, S. Gordeyev, A. Nightingale, and E. Jumper

Center for Flow Physics and Control
Department of Aerospace and Mechanical Engineering, University of Notre Dame,
Notre Dame, IN 46556, USA

Abstract

A two-dimensional, weakly-compressible shear layer with $M_1 = 0.78$, $M_2 = 0.15$ was computed using COBALT, a commercially-available full Navier-Stokes flow solver. The computed velocity field results were then used to compute thermodynamic flow-field data using a weakly-compressible model (WCM) developed at the University of Notre Dame. Comparison of results showed very-good match between the pressure fields computed using the WCM with the COBALT results, but serious discrepancies between the density and temperature fields. The discrepancies between the WCM and the COBALT results were investigated using an energy analysis.

Introduction

Airborne optical systems that are designed for maximum field of regard typically encounter shear-layers associated with separated flow fields at large look-back angles. At compressible flow speeds, these shear layers become optically active, seriously degrading the far-field irradiance distribution of a laser beam that transits the flow. The impact that shear-layer flows have on the utility of airborne optical systems makes them one of the most important types of flow fields for aero-optic investigations.

One of the first investigations directed towards determining the cause of the optical aberrations in compressible shear-layer flows is given in [1]. In [1] a “weakly compressible model” (WCM) was developed which combined the unsteady Euler equations with isentropic, adiabatic flow relations to determine thermodynamic flow properties from a pre-determined velocity field. The method was shown to be accurate for flows in which the shear-layer convective Mach number [2] was less than approximately 0.45; these flows can be considered “weakly compressible” in the sense that, although density variations are present, compressibility effects are not strong enough to influence the development of the underlying shear-layer velocity field. The decoupling of the velocity field from compressibility effects enabled the use of an incompressible discrete vortex method (DVM) [3, 4] to compute physically-realistic velocity fields for use with the WCM. Together, the DVM/WCM computational models showed that the large-amplitude aberrations caused by compressible shear layers were in large part the result of deep pressure wells associated with the vortical structures within the shear layer and their concomitant large-amplitude density variations. This result was a contentious outcome of the investigation, since previous studies suggested that the aberrations originated

primarily from the difference in the indices of refraction of the two flows undergoing mixing.

The conclusions of [1], and the accuracy of the WCM, have been demonstrated by the favorable comparison of DVM/WCM-computed results with aero-optic data measured in experimental shear flows [5, 6]. These experimental data consist, however, of optical data from which the density field can be inferred, and therefore provide only an indirect means of comparison with the temperature and density fields computed using the WCM. Further, the DVM, which was used to generate velocity fields for the WCM, is an inviscid computational method and, although shear layer development is primarily an inviscid process, the lack of modeling of viscous effects in the DVM/WCM models is still a limitation of the approach. Both of these limitations highlight the utility of comparing the WCM to a higher-level computational solution that includes viscous modeling. This paper describes a comparison of the WCM with COBALT, a commercially-available full Navier-Stokes flow solver

Weakly Compressible Model

The weakly-compressible model is designed to compute pressure, temperature and density fields from a pre-determined velocity field for "weakly compressible" flows in which development of the velocity field can be assumed to be decoupled from thermodynamic properties; for example, compressible shear-layers with low convective Mach numbers (cf below). The model is composed of the unsteady Euler equations, the ideal gas law, and an isentropic temperature relation:

$$\frac{\partial p}{\partial x} = -\rho\left[\frac{\partial u}{\partial t} + U\frac{\partial u}{\partial x} + V\frac{\partial u}{\partial y}\right] \tag{1}$$

$$\frac{\partial p}{\partial y} = -\rho\left[\frac{\partial v}{\partial t} + U\frac{\partial v}{\partial x} + V\frac{\partial v}{\partial y}\right] \tag{2}$$

$$T_S = T_{AB}\left(\frac{p}{p_\infty}\right)^{\left(\frac{\gamma-1}{\gamma}\right)} \tag{3}$$

$$p = \rho R T_S \tag{4}$$

The adiabatic static temperature distribution T_{AB} is determined at each point in the flow using the pre-determined velocity field:

$$T_{AB} = T_T - \frac{V^2}{2C_P} \tag{5}$$

The solution is started by setting the initial guess for the pressure field as $p(x,y) = p_\infty$, after which Eqs.(1) to (4) are iterated to convergence. The model assumes that the two

streams feeding the shear layer have the same total temperature T_T, and the initial adiabatic temperature distribution T_{AB} is computed using an assumed initial constant total temperature throughout the flow field. The final T_T distribution of the converged solution can, however, vary throughout the flow field due to local unsteady pressure variations, as discussed in greater detail below. A flow chart for the WCM solution procedure is given in Figure 1.

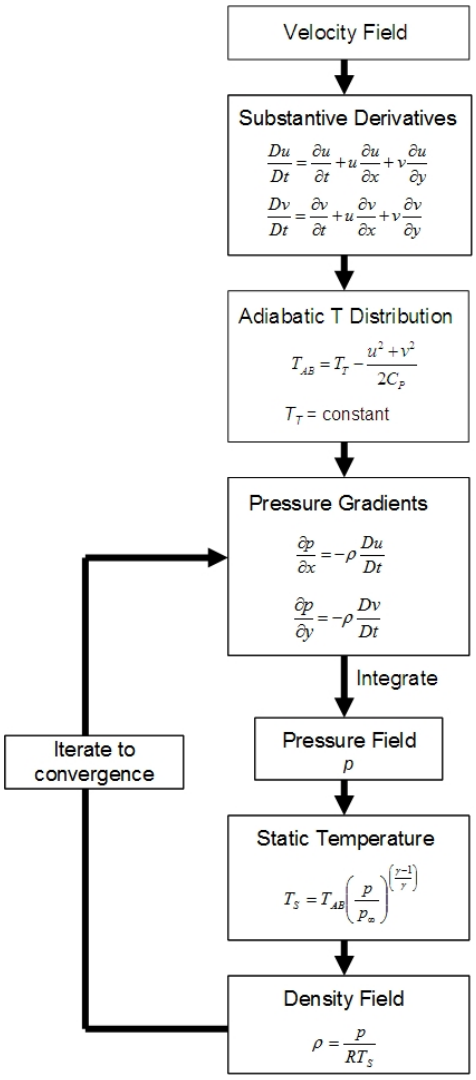

Figure 1: Flow chart for Weakly Compressible Model

Computational Shear-Layer Model

A two-dimensional shear-layer flow was computed using COBALT, which is an implicit, unstructured, compressible Navier-Stokes flow solver [7]. The modeled shear layer had a high-speed Mach number M_1 = 0.78, a low-speed Mach number M_2 = 0.15, a freestream static pressure of one atmosphere, and a constant total temperature T_T = 300 K

for both the high- and low-speed flows. These parameters give a shear-layer velocity ratio $r = U_2/U_1$ of 0.19 and density ratio $s = \rho_2/\rho_1$ of 0.90, and were chosen to model realistic aero-optic flow conditions similar to experimental flows reported in [5, 6, 8]. The convective Mach number for the shear layer was computed using Eqs. (6), (7) [2] giving $M_{C1} = 0.33$; this Mach number is sufficiently low that the flow can be considered "weakly compressible" and is therefore suitable for comparison to the WCM.

$$M_{C1} = (U_1 - U_C)/a_2 \tag{6}$$

$$U_C = \frac{a_2 U_1 + a_1 U_2}{a_1 + a_2} \tag{7}$$

The computational domain was designed to accurately model roughly the first 0.8 m of the shear-layer development. The size of the domain was 3 m x 5 m which was estimated as sufficiently large to ensure that the solution would not be influenced by the fixed flow conditions at the domain boundaries. The domain was meshed using an unstructured triangular mesh, with the smallest mesh size chosen to accurately resolve the smallest eddies that were expected to occur in the computational solution. The smallest eddies occur near the origin of the shear layer and can be estimated as the convection length Λ_n corresponding to the initial shear-layer natural frequency f_n:

$$\Lambda_n = \frac{U_{cn}}{f_n} \tag{8}$$

where U_{cn} is the shear-layer convection velocity, $U_{cn} = (U_1 + U_2)/2$. According to [9], f_n depends primarily upon the momentum thickness of the boundary layer feeding the high-speed side of the shear layer, and can be estimated from linear stability theory using:

$$\frac{f_n \theta}{U_1 / 2} = 0.036 \tag{9}$$

The initial shear-layer development was therefore established by defining an inlet velocity profile that modeled the boundary layer from an upstream splitter plate. The boundary-layer parameters chosen for the high-speed flow were boundary layer height $\delta = 5$ mm and momentum thickness $\theta \sim 0.5$ mm; these parameters matched measurements of the splitter-plate boundary layer made in the Compressible Shear-Layer Wind Tunnel at the University of Notre Dame [6, 8]. Using Eqns (8) and (9), these boundary-layer parameters give $f_n \sim 10$ kHz, and $\Lambda_n \sim 14$ mm. To ensure that the smallest eddies would be resolved with a comfortable margin of safety, a minimum grid size of 0.5 mm was used along the first 0.8 m of the computational domain. A diagram of the computational grid, including solution boundary conditions, is shown in Figure 2. The convention of flow from left to right with the high-speed flow at the top is maintained in all figures shown in this paper.

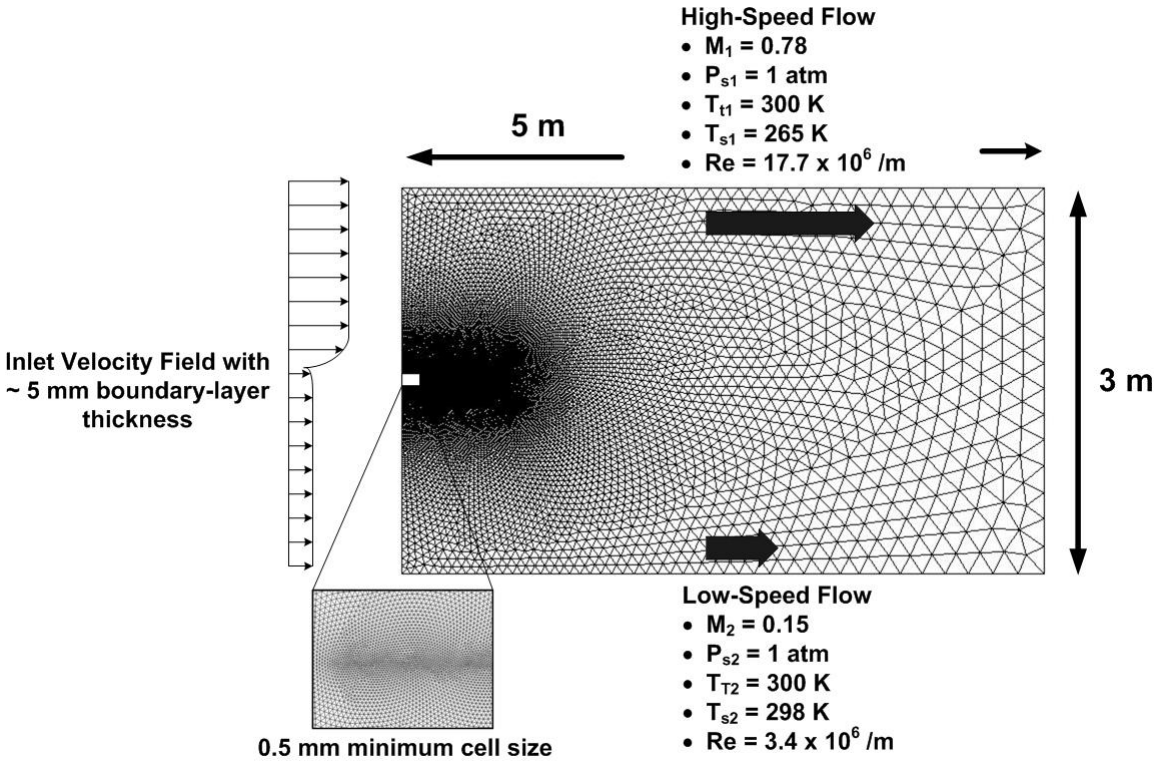

Figure 2: Computational grid and boundary conditions for shear-layer model

Shear-Layer Velocity Field

The computational solution was run until starting transients had decayed, after which time-averaged velocity fields in the shear layer were computed. Figures 3 (a) and (b) show time-averaged and rms velocity profiles nondimensionalized by the shear-layer vorticity thickness δ_ω, Eq. (10), at several locations within the computed solution. The figures show that the computational results closely match the profile shape for the canonical shear layer.

$$\delta_\varpi = \frac{u_1 - u_2}{(\partial u / \partial y)_{\max}} \tag{10}$$

The vorticity thickness growth in the computed velocity field is plotted in Figure 4. The figure shows some nonlinearity in the growth of the computed δ_ω for x > 0.6 m, which is near the end of the finely-meshed region of the computational domain. The figure includes a theoretical estimate for the δ_ω growth [10] which compares well to the computational solution. Overall, the velocity field results in Figures 3 and 4 show that the computed shear-layer velocity field compares reasonably well to canonical forms and theoretical predictions.

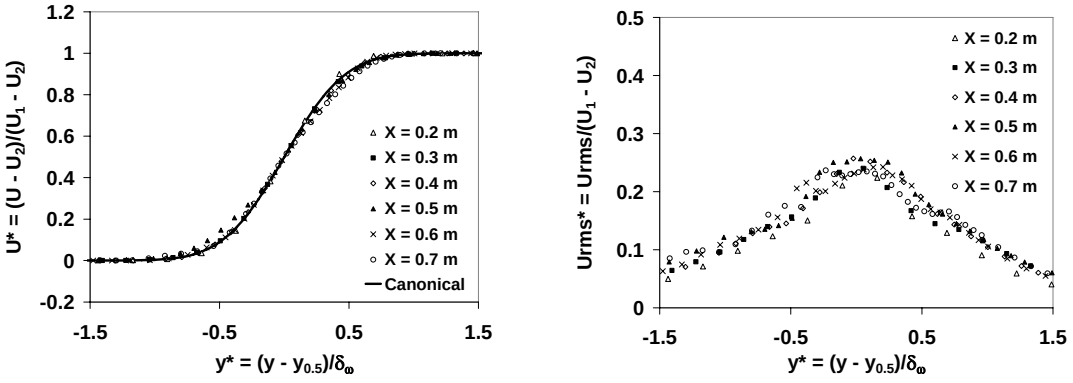

(a) **(b)**

Figure 3: (a) Nondimensional time-average and (b) rms velocity profiles in computed shear layer

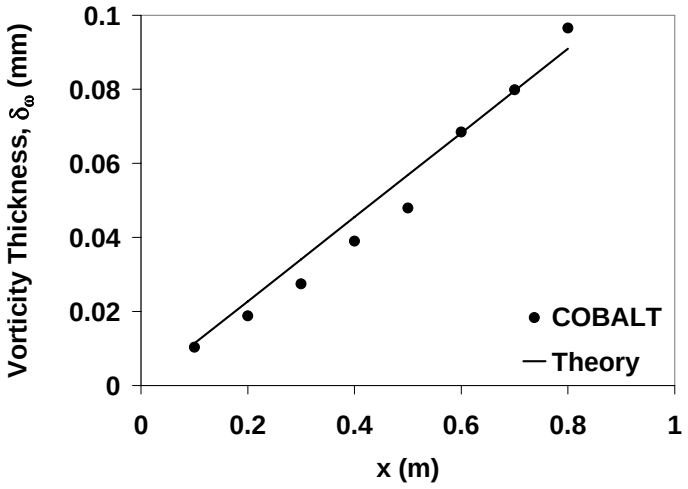

Figure 4: Shear-layer vorticity thickness development

Comparison of Navier-Stokes Solution to WCM

The shear-layer velocity field computed using COBALT was used to compute pressure, temperature and density fields using the WCM, Figure 1, which were then compared to the thermodynamic results of the COBALT full Navier-Stokes solution. The vorticity field for the solution time step used in the comparison is shown in Figure 5, which shows several vortices within the comparison region. As shown in the figure, the comparison region was limited to $x < 0.6$ where the velocity field most accurately represents that for a canonical shear layer, Figure 4.

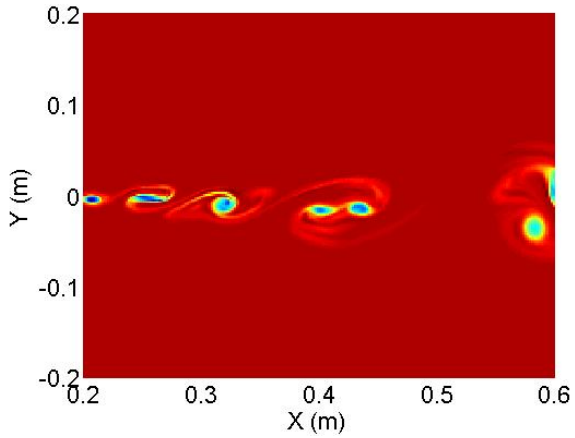

Figure 5: Vorticity field for solution time step used to compare COBALT and WCM

Pressure distributions over the comparison region computed using COBALT and the WCM are shown in Figure 6. The pressure fields show deep pressure wells at the locations of the shear-layer vortex cores shown in the vorticity field in Figure 5; this result agrees with the predictions in [1] of the existence of these pressure wells. A plot of the computed pressure distributions down the centerline of the computational domain (at y = 0) is shown in Figure 7. Overall, Figures 6 and 7 show very good agreement between COBALT and the WCM in terms of the computed pressure fields.

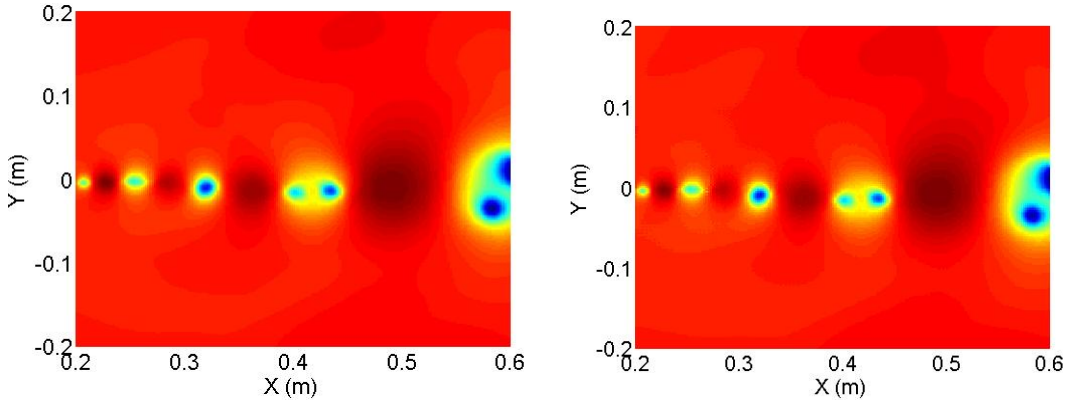

(a) **(b)**

Figure 6: Pressure fields computed using (a) COBALT and (b) WCM

The almost exact match between the WCM pressure field and the results computed using a full Navier-Stokes solver validates the most contentious idea presented in [1], which is that deep pressure wells exist in the shear-layer flow field at the locations of the shear-layer vortices. The good comparison also supports the idea that the WCM can be overlayed on a pre-determined velocity field to accurately compute thermodynamic properties. Based on the good results of the pressure-field comparison, attention next focused on comparing the temperature and density fields.

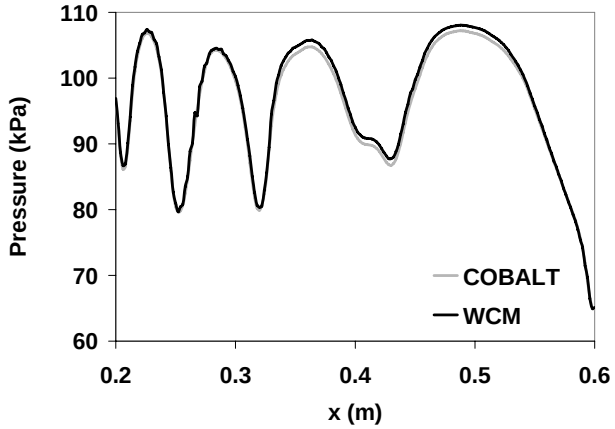

Figure 7: Pressure distribution along centerline of computational domain, at y=0.

Static temperature and density fields computed by COBALT and the WCM for the same velocity field are compared in Figure 8. The figures show that depressions in the static temperature and density also exist at the vortex core locations. The agreement between COBALT and the WCM is relatively good in the region of the vortex cores; however, the figure generally shows a significant difference between the two methods in the way in which the T_S and ρ fields merge between the high- and low-speed flows. In particular, the COBALT solution shows very sharp, rapid changes in T_S and ρ between the high- and low-speed flows while the WCM solution shows very gradual changes; this difference is noticeable throughout the flow but is particularly apparent in the braid regions between the vortices.

Optical path differences, OPD's, were also computed from the COBALT and WCM density fields using:

$$OPL = \int n(t, x, y)dy \tag{11}$$

and

$$OPD = OPL - \overline{OPL} \tag{12}$$

where

$$n(t,x,y) = 1 - K_{GD}\,\rho(t,x,y) \tag{13}$$

In Eq.(13), a value of 2.25 x 10^{-3} kg/m^3 was used for the Gladstone-Dale constant to model the propagation of 1 μm wavelength radiation in air. OPD distributions over the comparison region are shown in Figure 9. The OPD's shown in the figure are marginally larger than OPD's given for experimental studies reported in [5, 6, 8]. It should be noted however, that the freestream static pressure used for the computational results in Figure 9 was significantly larger than for the experimental data in [5, 6, 8] and that, when the

computational data were scaled to the same p_∞ as the experimental data then comparable OPD's were obtained.

Figure 9 shows reasonably good comparison between the OPD distributions computed using the COBALT and WCM density fields, but an approximately 30% difference in the two OPD's in regions that correspond to the braids between the shear-layer vortices. As such, the differences in the density fields computed using COBALT and the WCM lead to significant differences in the corresponding estimates of the flowfield optical aberrations.

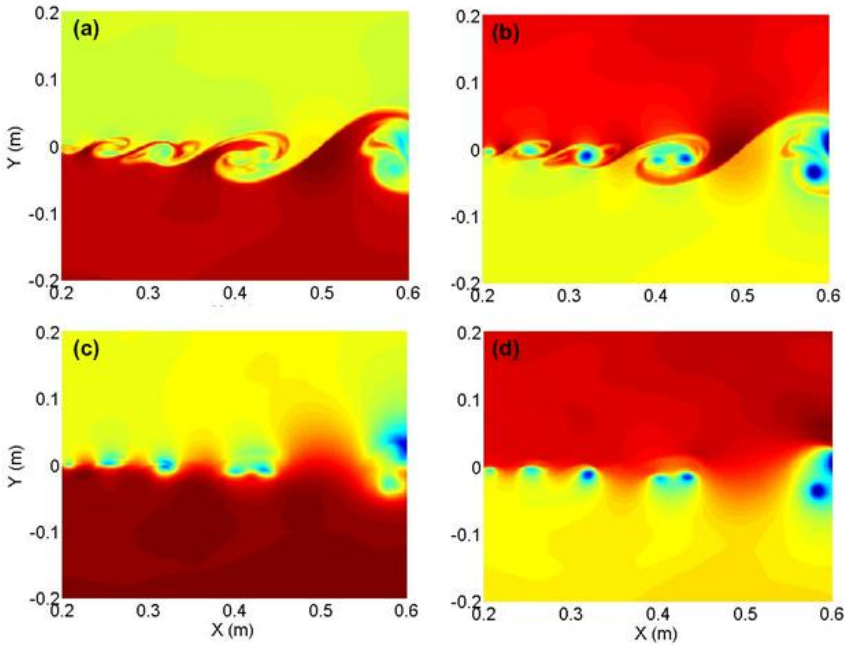

Figure 8: (a) Temperature and (b) density fields computed using COBALT, and using WCM (c and d).

Energy Equation and Total Temperature

The good comparison between pressure distributions, but poor agreement between temperature and density fields for COBALT and the WCM suggested that an explanation for the discrepancy could be obtained from examination of the energy equation. The differences between the two solutions appear to be primarily caused by differences in the computation of the temperature fields, which is determined by the energy equation, whereas the density variations arise for the most part from temperature differences via the equation of state.

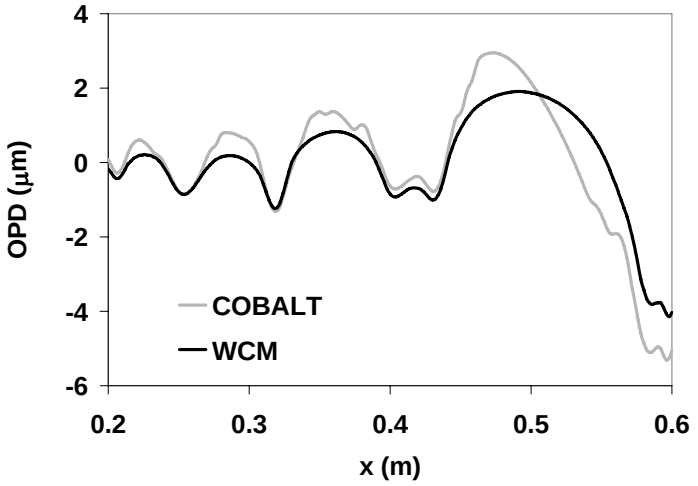

Figure 9: OPD's for COBALT and WCM solutions.

The total energy equation in differential form, with the work contributed by body forces neglected, is shown in Eq. (14). The terms on the left-hand side make up the substantial derivative of the total energy, that is, the rate of change of internal plus kinetic energy of a point moving with the flow. The source terms on the right hand side consist of, in order, the net heat transfer, the work of viscous forces and the work of pressure forces. Since there is no heat transfer across the boundaries of the computational domain, heat transfer only serves to smooth out temperature variations that are produced by other source terms within the flow itself. As such, heat transfer terms can be neglected from the energy equation since heat transfer alone cannot produce the sharp temperature gradients observed in the COBALT temperature field in Figure 8; in fact, heat transfer should produce the opposite effect of a smoothed-out temperature distribution.

$$\frac{\partial}{\partial t}\left[\rho\left(C_v T_S + \frac{V^2}{2}\right)\right] + \vec{\nabla}\cdot\left[\rho\vec{V}\left(C_v T_S + \frac{V^2}{2}\right)\right] = -\vec{\nabla}\cdot\vec{q} + \vec{\nabla}\cdot\left(\bar{\bar{\tau}}\cdot\vec{V}\right) - \vec{\nabla}\cdot\left(p\vec{V}\right) \qquad (14)$$

Using the COBALT solution for the velocity field, the viscous work term was computed within the comparison region. As shown in Figure 10, the viscous work is almost nonexistent in the braid regions between the vortices; furthermore, if the path of a fluid particle is integrated over Figure 10, then generally only very small temperature variations are produced, and these occur only very close to the domain centerline, y=0. These two results show that the viscous work term can be neglected for the shear flow. The argument that viscous work is small for the shear-layer flow under investigation is further supported by the results of a matched-static temperature calculation of a similar shear-layer flow, presented later.

With heat transfer and viscous work terms removed, the energy equation reduces to the form shown in Eq.(15):

$$\frac{D}{Dt}\left[\rho\left(C_v T_S + \frac{V^2}{2}\right)\right] = -\vec{\nabla}\cdot\left(p\vec{V}\right) \qquad (15)$$

This equation can be manipulated into a simple relation between temporal changes in total temperature and pressure [11]:

$$\frac{DT_T}{Dt} = \frac{1}{\rho C_P}\frac{\partial p}{\partial t} \tag{16}$$

Equation (16) shows that total-temperature changes are localized to regions of large pressure variations. In particular, changes in T_T should be expected to occur within the deep pressure wells associated with the shear-layer vortices; outside of the vortex cores, T_T should be relatively constant.

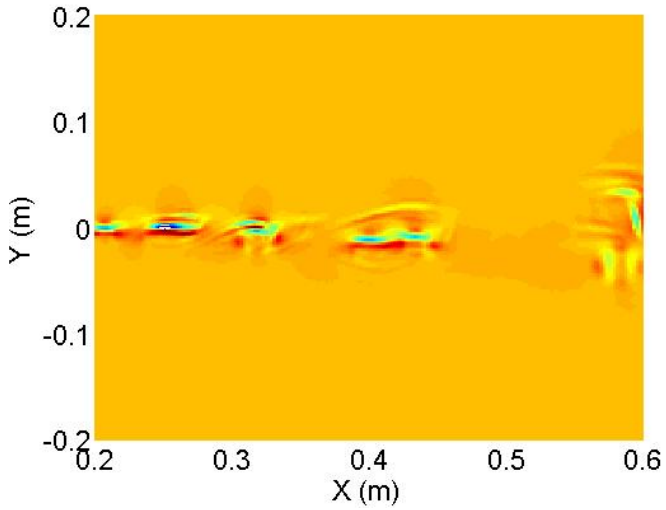

Figure 10: Viscous work, $\vec{\nabla}\cdot\left(\bar{\bar{\tau}}\cdot\vec{V}\right)$, within the comparison region.

The total-temperature fields computed using COBALT and using the WCM are compared in Figure 11. As predicted by the energy-equation analysis given above, the WCM T_T field is essentially constant, with only small localized depressions in T_T occurring at locations corresponding to the deep pressure wells at the centers of the shear-layer vortices, as indicated by Eq. (16). The COBALT T_T field also shows regions of depressed T_T corresponding to the vortex core locations; however, the COBALT T_T field also shows generally very large differences and large gradients in T_T across the shear layer region, presumably at the interface between the fluids in the high- and low-speed flows, and including the braids between the vortices. These large differences and gradients are more visible in Figure 12, which shows a three-dimensional view of the T_T fields plotted in Figure 11. In fact, some of the largest T_T gradients in the COBALT solution occur in regions that are considerably displaced in the y direction from the domain centerline, where both velocity and pressure gradients are small. These large and sharp variations across the shear layer cannot be explained by the energy-equation analysis given above.

Further insight into the results can be obtained by examining the total temperature behavior in the braids between the vortices. As shown by Eq.(16), total temperature

should be relatively constant within the braid regions where the pressure excursions are small, giving:

$$T_T = T_S + \frac{V^2}{2C_P} = \text{constant} \tag{17}$$

Figure 13 shows static-temperature T_S and kinetic-energy $V^2/2C_P$ distributions along two cuts through the shear layer at locations corresponding to the braids at $x = 0.37$ m and $x = 0.5$ m. The figure shows that the kinetic energy variation (and concomitantly, the velocity variation) through the braids changes very smoothly between the high and low-speed flows. The figure also shows that the corresponding static-temperature variation through the braid for the WCM solution is also very smooth, and that T_S changes in such a way that the addition of T_S and the kinetic energy produces essentially constant T_T (except for a small "hump" caused by the pressure variation in the braid, as shown in Figures 6 and 7). On the other hand, the COBALT static temperature distribution through the braid regions changes very abruptly, and it is apparent from Figure 13 that it is the abrupt changes in T_S across the braid region that produce the abrupt changes in T_T in Figures 11 and 12.

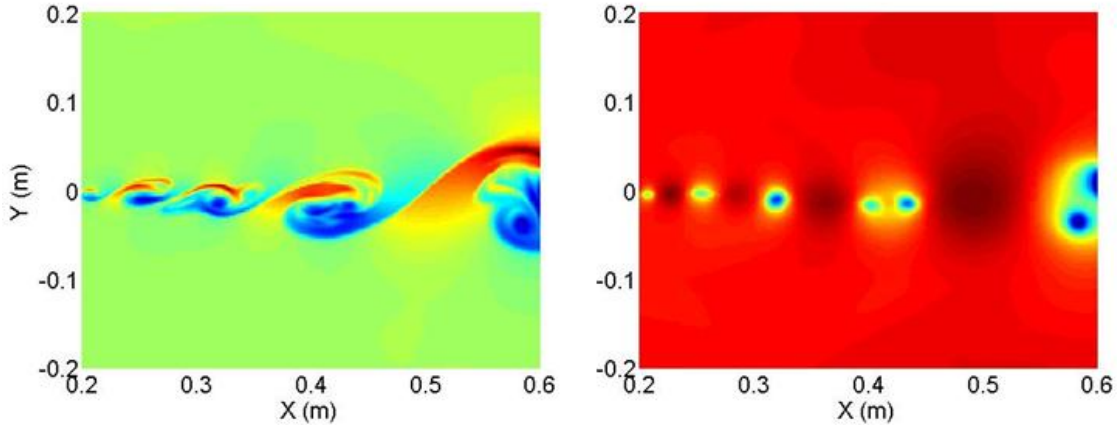

(a) **(b)**

Figure 11: Total temperature distributions computed using (a) COBALT and (b) WCM

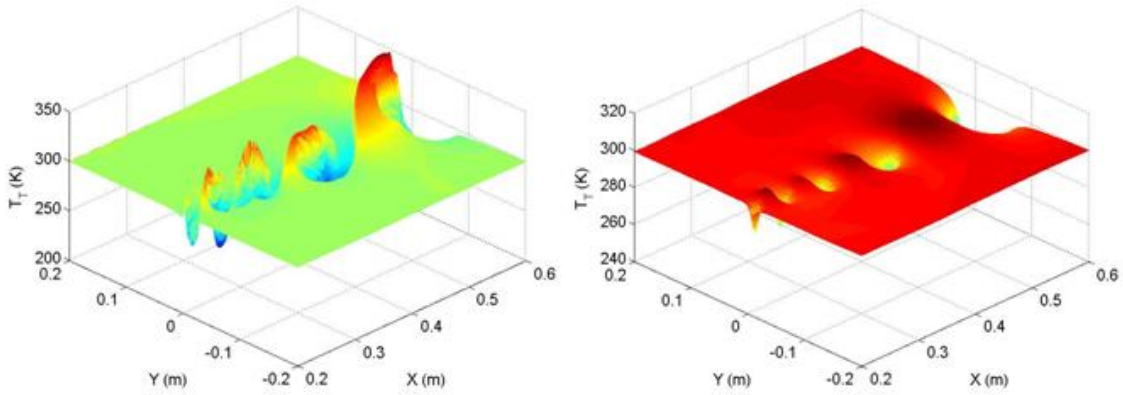

(a) **(b)**

Figure 12: Relief view of total temperature distributions computed using (a) COBALT and (b) WCM

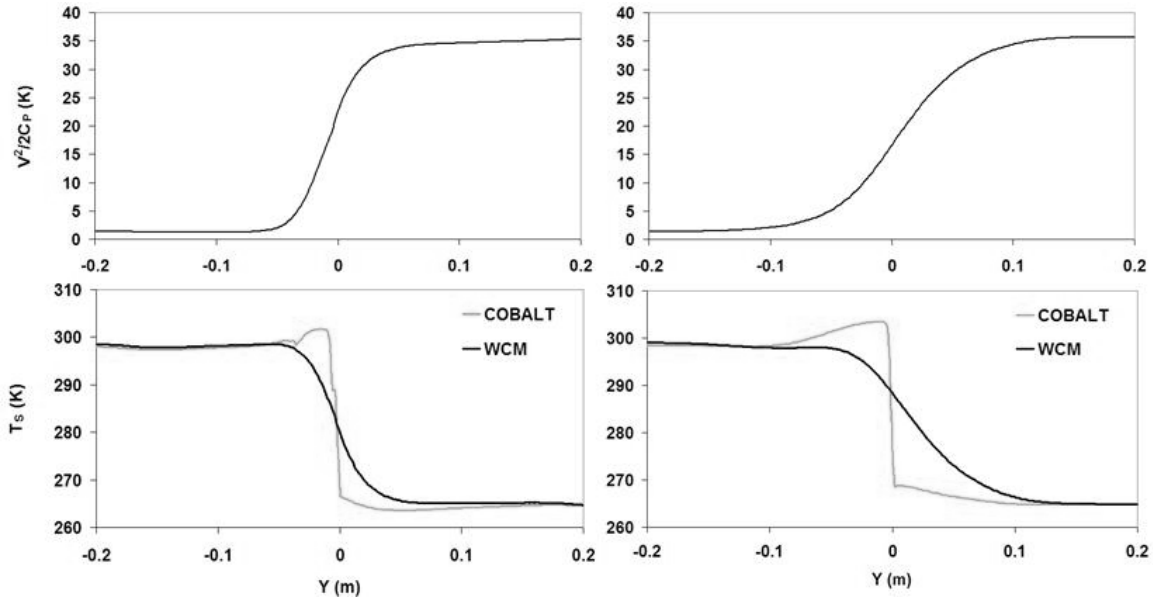

(a) **(b)**

Figure 13: Kinetic-energy and static-temperature contributions to the total temperature along cross-stream cuts in shear-layer braids at (a) x = 0.375 m, and (b) x = 0.5 m

Simulated and Experimental Schlierens

The differences between the COBALT and WCM solutions are in the computed temperature and density fields. These discrepancies are difficult to resolve using experimental data since it is difficult to directly measure temperatures in compressible

experimental flows. Instead, the computational data has been compared to optical measurements where the density field can be inferred from, for example, integrated optical path differences as shown in Figure 9. Another optical measurement technique, which produces spatially resolved information on the density field, is Schlieren photography.

Simulated Schlieren photographs of the computational flow field are shown in Figure 14 for the COBALT and WCM solutions. The simulated Schlieren figures were computed as the gradient of the computed density fields, with the gradient direction and figure shading chosen to produce an effect similar to experimental photographs shown in Figure 15. The simulated Schlierens for the COBALT and WCM solutions show distinct differences, primarily that the WCM Schlieren shows strong density gradients around the shear-layer vortices only, while the COBALT Schlieren shows strong gradients in the braid regions as well; these differences correspond to the differences in the computed density fields already shown in Figure 8.

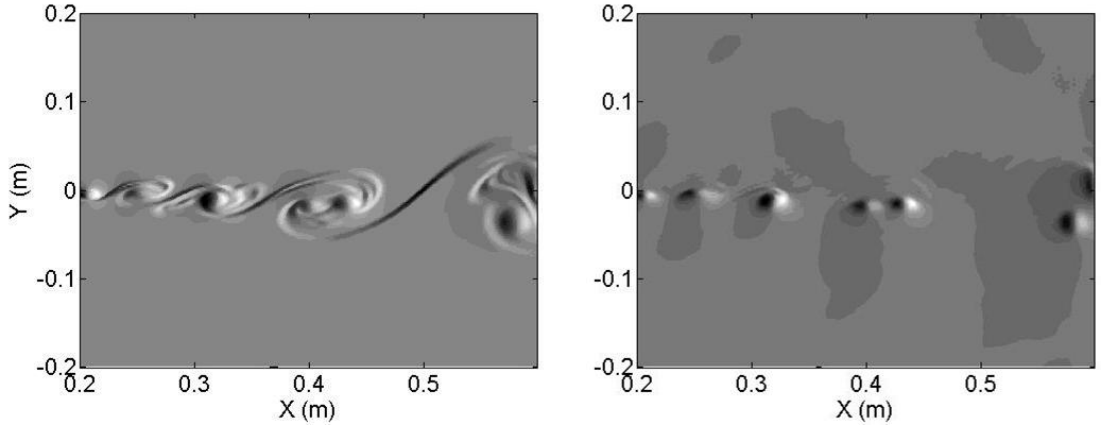

(a) **(b)**

Figure 14: Simulated Schlieren photographs of density fields computed using (a) COBALT and (b) WCM

Figure 15 (a) shows an experimental Shlieren photograph for a M = 0.6 compressible shear layer with matched T_T streams, similar to the type of flow modeled in this investigation, and in (b), a low-speed incompressible shear layer that mixes two fluids with two different indices of refraction. The difference between these two Schlieren photographs is important in the sense that in Figure 15(a) density variations are produced by compressibility effects while in (b) the shear layer merely mixes two streams with initially different densities. Comparison of Figure 14 to Figure 15 shows that the WCM solution shows much more similarity to the experimental M = 0.6 shear layer with matched T_T streams, while the resolved braids in the COBALT Schlieren appear more similar to the incompressible mixing-layer Schlieren in Figure 15(b).

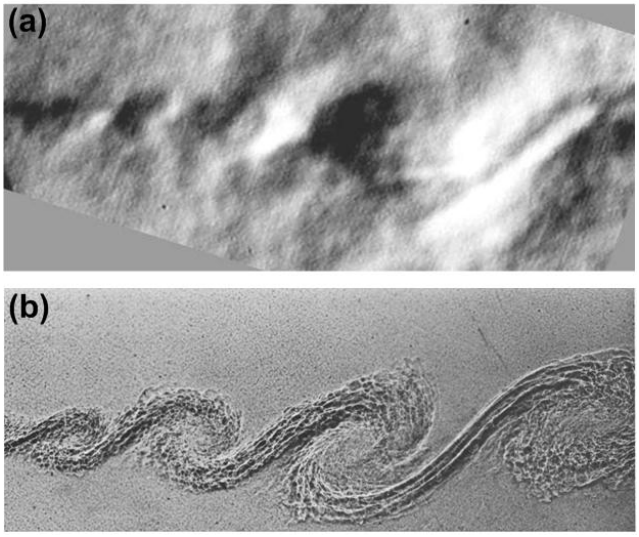

(a) (b)

Figure 15: Experimental Schlieren photographs for (a) a M = 0.6 shear layer with matched T_T in the upper and lower flows, and (b) a low-speed incompressible shear layer that mixes two fluids with different indices of refraction.

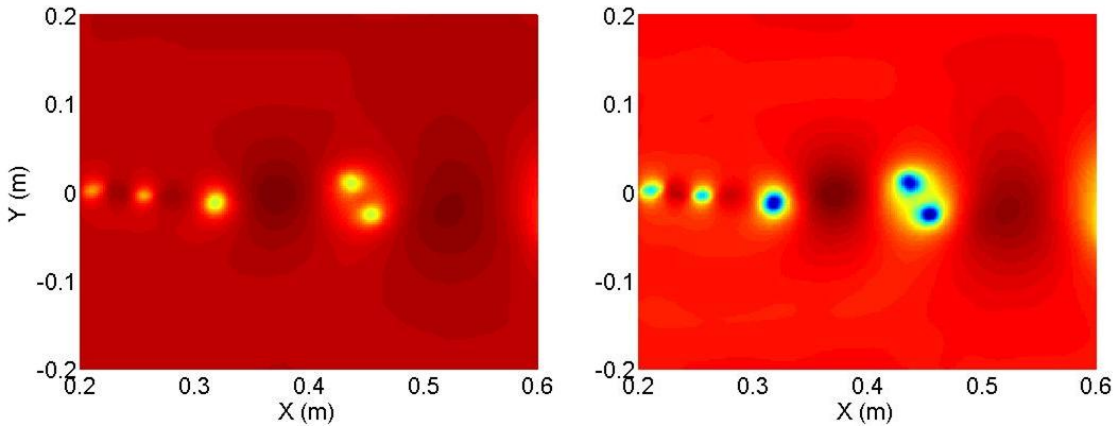

(a) (b)

Figure 16: COBALT solution for (a) static-temperature and (b) density fields for shear layer with matched T_S and all other boundary conditions the same as shown in Figure 2.

Shear Layer with Matched Static Temperature

The Schlieren photographs and the total temperature arguments presented above show that the COBALT solution gives the appearance of mixing two fluids of different T_S, without accounting for the exchange of energy between kinetic and internal energies that maintains constant T_T in the braid regions according to Eq. (17). An alternate explanation is that viscous work is an important source of local temperature variations in the COBALT calculation, and that the WCM may be incorrectly neglecting the viscous

work terms. This possibility was investigated by computing a shear-layer solution for two streams with matched static temperatures T_S. The computational grid and boundary conditions for the solution were exactly the same as for the matched-T_T solution shown in Figure 2, except that the static temperature of the upper and lower flows were both set equal to 300 K.

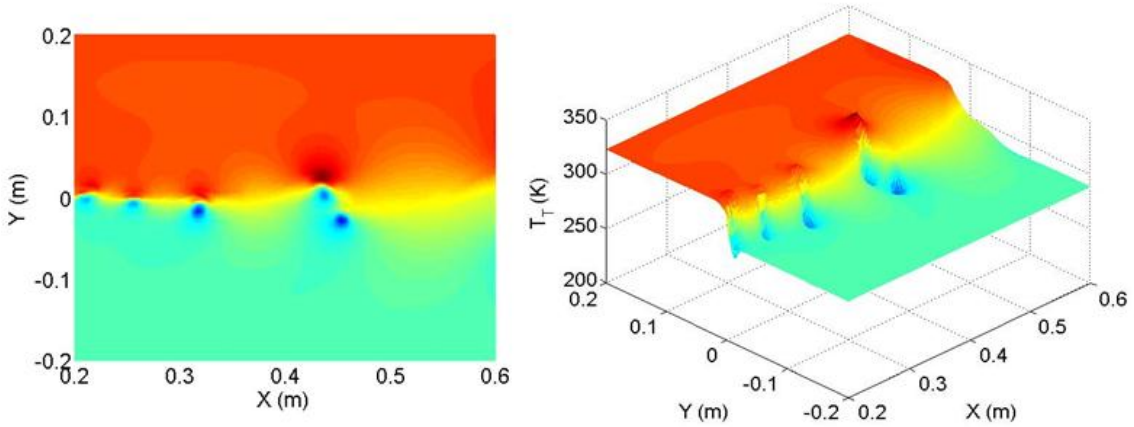

(a) **(b)**

Figure 17: (a) Contour and (b) relief views of COBALT T_T field for shear layer with matched T_S.

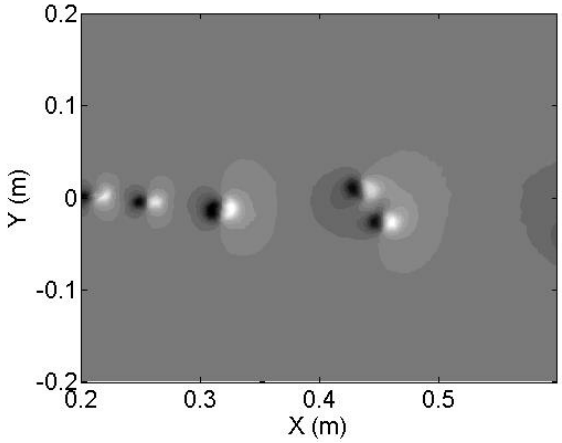

Figure 18: Simulated Schlieren for COBALT solution for shear layer with matched T_S.

The COBALT solution for T_S and ρ for the matched-T_S solution is shown in Figure 16. Although the figure shows localized T_S and ρ excursions in the vicinity of the shear-layer vortices, in general, the T_S and ρ fields are smooth with only gradual changes, particularly within the braid regions. However, if the sharp T_S and ρ variations in the matched T_T solution were caused by localized heating by viscous work terms, then one would expect to see similar localized heating in the matched T_S solution in Figure 16. This is because viscous work arises from the velocity field, and the velocity fields for the matched T_S solution has similar characteristics to the velocity field for the matched T_T

solution. One possible explanation is that localized heating from viscous work is exactly offset by adiabatic cooling via Eq.(17) thus producing the smooth T_S field of Figure 16; however, this would be very coincidental. Instead the much more likely explanation is that viscous work in the COBALT solution is negligible, and that the simple mixing appearance of the COBALT solution for the matched T_T solution is masked in the matched T_S solution because the two flows have the same T_S. The T_T field for the matched T_S solution is shown in Figure 17, which shows gradual changes in the T_T distribution, particularly in the braid regions. Figure 18 shows a simulated Schlieren computed using the density field from the COBALT matched T_S solution; this simulated Schlieren is very similar in appearance to the simulated Schlieren computed using the WCM solution for matched T_T in Figure 15, and further illustrates the absence of localized heating due to viscous effects in the COBALT solutions.

Conclusions

The pressure fields computed using COBALT, a full Navier-Stokes flow solver, show the large pressure wells and concomitant density depressions at the shear-layer vortex core locations that were predicted in [1]. These results further validate the analysis given in [1] showing that the primary mechanism for optical aberrations in a weakly-compressible shear layer are pressure and density variations associated with the shear-layer vortices.

The velocity field computed using COBALT was also used to compute pressure, temperature and density fields using the WCM. While the pressure fields computed using the WCM and COBALT showed very good agreement, the temperature and density fields showed significant discrepancies. In particular, the COBALT solution showed sharp gradients in temperature and density at the boundary between the high- and low-speed flows; this sharp delineation between the high- and low-speed flows resembled the kind of density field that is produced by simple mixing of two fluids of different densities, as if temperature was treated as a passive scalar with adiabatic heating and cooling effects, Eq. (17) neglected. Similar effects have been noticed in other investigations of weakly-compressible shear layers that used other compressible Navier-Stokes flow solvers. Comparison of the two methods using the energy-equation showed that the sharp changes in temperature evident in the COBALT solution could only be produced by localized heating due to viscous forces; however, an analysis of the velocity field showed that viscous work was small, as did a computation with matched static temperatures. As such, it is difficult to give a physical explanation for the large T_S and ρ gradients that appear in the COBALT solution, although further investigations should be carried out.

References

[1] Fitzgerald, E. J. and Jumper E. J., "The optical distortion mechanism in a nearly incompressible free shear layer," *Journal of Fluid Mechanics*, Vol. 512, 2004, pp. 153-189.

[2] Papamoschou, D., and Roshko, A., "The compressible turbulent shear layer: an experimental study," *Journal of Fluid Mechanics*, Vol. 197, 1988, pp. 453-477.

[3] Hugo, R.J, "Quantifying the Spatio-Temporal Effects of Optically-Active Turbulent Flowfields on a Coherent Optical Wave," Ph.D. Dissertation, Dept. of Aerospace and Mechanical Engineering, Univ. of Notre Dame, Notre Dame, IN, 1995.

[4] Nightingale, A., Gordeyev, S., Siegenthaler, D., Wittich, D., and Jumper, E., "Computed Aero-Optic Characteristics of a Free Shear Layer using the Weakly-Compressible Model," DEPS Beam Control Conference, Monterey, CA, Mar, 2006.

[5] Hugo, R. J, Jumper, E. J., Havener, G., and Stepanek, C., "Time-resolved Wave Front Measurements Through a Compressible Free Shear Layer," *AIAA Journal*, Vol. 35, No. 4, 1997, pp. 671-677.

[6] Rennie, R. M., Duffin, D. A., and Jumper, E. J., "Characterization and Aero-Optic Correction of a Forced, Two-Dimensional, Weakly-Compressible Shear Layer," AIAA 2007-4007, Jun., 2007.

[7] Strang, W. Z., Tomaro, R. F., and Grismer, M. J., "The Defining Methods of $Cobalt_{60}$: A Parallel, Implicit, Unstructured Euler/Navier-Stokes Flow Solver," AIAA 1999-0786, Jan, 1999.

[8] Rennie, R. M., Siegenthaler, J. P., and Jumper, E. J., "Forcing of a Two-Dimensional, Weakly-Compressible Subsonic Free Shear Layer," AIAA 2006-0561, Jan., 2006.

[9] Ho, C. M., and Huang, L. S., "Subharmonics and vortex merging in mixing layers," *Journal of Fluid Mechanics*, Vol. 119, 1982, pp.443-473.

[10] Dimotakis, P.E., "Two-Dimensional Shear-Layer Entrainment," *AIAA Journal*, Vol. 24, No. 11, 1986, pp. 1791-1796.

[11] Anderson, Jr., J. D., *Modern Compressible Flow*, 3rd edn., McGraw-Hill, 2003.